Analysis of Coronal Holes in the Descending Phase of Cycles 23 and 24 Using EUV and Magnetic Field Data

Andrea Minot[1], Jonathan Lee[2], Xudong Sun[3]
[1]*Brown University, Providence, RI 02912*
[2]*University of Colorado Boulder, Boulder, CO 80309*
[3]*Institute for Astronomy, University of Hawai`i at Mānoa, Honolulu, HI 96822*

In this study, we analyze area and magnetic properties of coronal holes during the descending phases of solar cycles 23 and 24 using a semi-automated method of intensity thresholding on extreme ultraviolet imagery. Comparing these two cycles will enable us to not only shed light on the abnormalities of cycle 23 but also to see if the same trends persist into the ongoing cycle 24. We attempt to reaffirm that cycle 23 has a weak dipole component and compare it to that of cycle 24. Cycle 24 has a higher percentage of polar coronal hole area and higher northern magnetic field values and is discussed in further detail in this paper. These results will be useful in exploring solar cycle properties as well as in the development of coronal hole modeling.

INTRODUCTION

Coronal holes (CHs) are regions on the sun with a strong monopolar magnetic field component and are a direct cause of fast solar wind as well as increased geomagnetic activity at Earth. Studying CHs is crucial to improving our space weather forecasting techniques as well as understanding the solar cycle as a whole. In this study, we are particularly interested in the latter.

Of the 24 solar cycles (we are currently in solar cycle 24), cycle 23 stands out due to its many abnormalities compared to previous cycles. In particular, the minimum phase between cycle 23 and 24 is peculiar because the sun's polar magnetic fields were approximately 40% weaker than the strength of the preceding three cycles accompanied by a 20% decreased total polar CH area coverage (Wang 2009.) We can investigate the period before minimum, also known as the descending phase, to see if this trend continues. By comparing magnetic field values and CH areas and locations from the descending phase of cycle 23 to the succeeding descending phase (of cycle 24), we may better our understanding of cycle 23, better our predictions for cycle 24, and for future cycles.

Our study investigates this topic in two parts. The first part examines CH sizes, locations, and magnetic field environments during the descending phases of solar cycle 23 and 24. We use Solar and Heliospheric Observatory/Extreme ultraviolet Imaging Telescope (SOHO/EIT) and Solar Dynamic Observatory/Atmospheric Imaging Assembly (SDO/AIA) data to determine CH region sizes and locations and Michelson Doppler Imager (MDI) as well as Helioseismic and Magnetic Imager (HMI) magnetogram data to study the magnetic field. The second part compares the actual CH regions obtained from SOHO/EIT and SDO/AIA imagery to ones simulated using the Potential Field Source Surface (PFSS) model with HMI data as input. This comparison between the two cycles and between the actual data and the modeled data, will not only allow us to search for preemptive indicators of solar cycle strength, but will allow us to better our modeling techniques.

METHODOLOGY

In this study, we are interested in the descending phases of cycles 23 and 24. To determine the span of these time periods, we plotted monthly sunspot number (SSN) of cycles 23 and 24 and normalized the vertical axis zero-to-one. We then chose the most recent data we have from cycle 24 as our end point and went backwards two years. We defined this to be the descending phases of each cycle and the resultant time period spans from Carrington rotation (CR) 1994 to 2021 (September 9, 2002 to September 14, 2004) in cycle 23 and CR 2159 to 2186 (January 4, 2015 to January 10, 2017) in cycle 24. A Carrington rotation is used as a unit of time taken for the sun to complete one rotation. The mean synodic rotation rate is 27.2753 days (WSO, Stanford.) Synoptic maps of the solar surface are made by imaging multiple ~15° longitudinal strips at the solar prime meridian and splicing them together over the course of one CR. The CR synoptic map data that we used was retrieved from Space Weather Lab at George Mason University and Stanford University. We were interested in the extreme ultraviolet (EUV) synoptic maps and, in particular, the 195 Å range for SOHO/EIT imagery and the 193 Å range for SDO/AIA imagery. In these wavelengths, CHs appear as dark regions making them relatively easy to visually see. The small differences in wavelength between 195 Å and 193 Å is unlikely to cause significant differences in CH detection (Hamada 2018). We also used processed HMI synoptic maps, however, the resolutions of the (HMI) data (360 pixels by 180 pixels) was different from EUV data (3600 pixels by 1800 pixels) meaning we had to write Python code to rescale and interpolate all the HMI synoptic maps to be the same dimensions as the EUV data. For MDI and EIT data, we scaled both to be 3600 by 1800 pixels as well. In addition, for some of the CR synoptic maps, only degree latitudes were available meaning we had to convert to sine latitude using loops in Python.

Our method of CH detection is semi-automated and was revised several times to be more automated and objective. Previous research has been done using automated methods of CH detection (e.g., Lowder *et al.* 2014 and Krista & Gallagher 2009), and we replicate some of the techniques in this study. Using the EUV data, we first defined an intensity threshold corresponding to the intensity values of CHs and quiet sun regions in each individual synoptic map. We did this by choosing a partial field of view

(FOV) region in the EUV imagery and creating a histogram of intensity values within that region. This method was first used by Krista & Gallagher (2009) to define CH regions and later replicated by Lowder *et al.* (2014). We chose a FOV that would show a clear bimodal distribution in the histogram. Figure 1 shows an EUV synoptic map of CR 2182 (from solar cycle 24) with an example of a partial FOV box overlaid. The color bar is in arbitrary units of intensity.

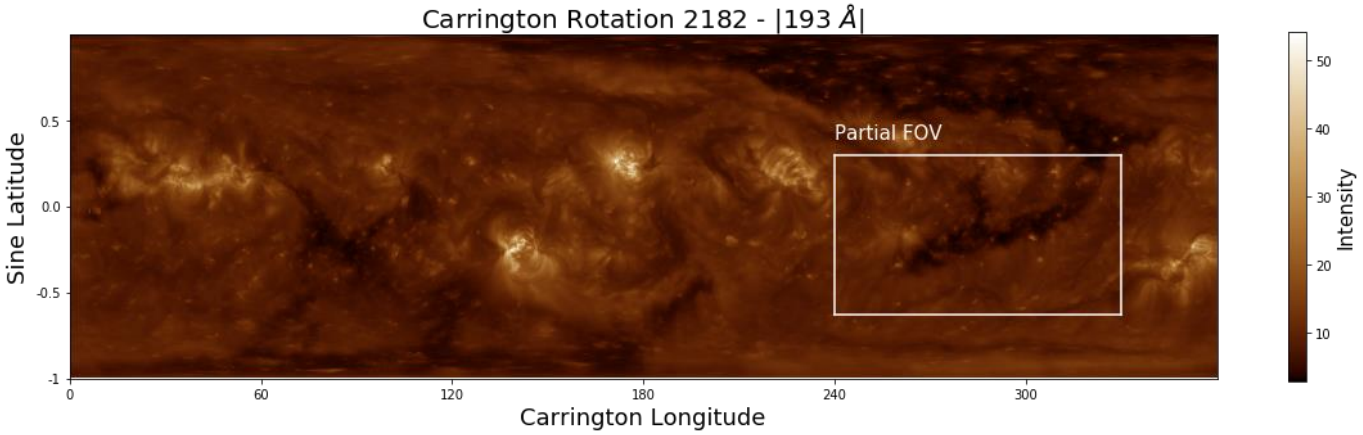

Figure 1: An extreme ultraviolet image of the solar surface during Carrington rotation 2182. The box encloses a chosen partial field of view (FOV) to give samples of different intensity values. This will optimally result in a histogram with a bimodal distribution. The intensity threshold used to contour coronal hole regions can then be obtained from this histogram.

Figure 2 shows the histogram created from the intensity values of the pixels inside the partial FOV. The lower intensity peak represents the CH region while the higher intensity region represents quiet sun regions. The local minimum between these two peaks, thus, is our chosen intensity threshold. Each synoptic map will have a unique threshold corresponding to the AIA or EIT imagery's different intensity scaling and to the solar surface environment during that Carrington rotation. Then, with each calculated intensity threshold, we contoured regions of intensity below this threshold defined to be CH regions. An example of these contours on top of EUV imagery is shown in Figure 3.

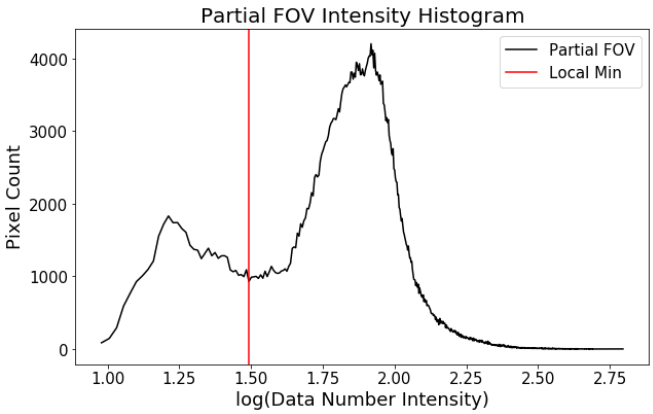

Figure 3: A histogram created from the intensity values within the partial FOV. There is a bimodal distribution, the higher intensity peak represents quiet sun regions while the lower intensity peak represents coronal hole regions. The local minimum between these two peaks (in red) is the threshold we use to contour coronal holes.

Filaments also appear in the contoured regions because they have a lower intensity in EUV imagery compared to the background sun. Finding a method or threshold to analytically distinguish between CHs and filaments is an area of ongoing study, however, we decided to adopt a method used by Lowder *et al.* (2014) because it was within our capabilities and produced favorable results. This method involved creating a histogram of the MDI/HMI magnetic field values within a contoured region. In CH regions, the magnetic field values are expected to be primarily positive or negative while in a filament channel region, the magnetic field should show a relative balance between

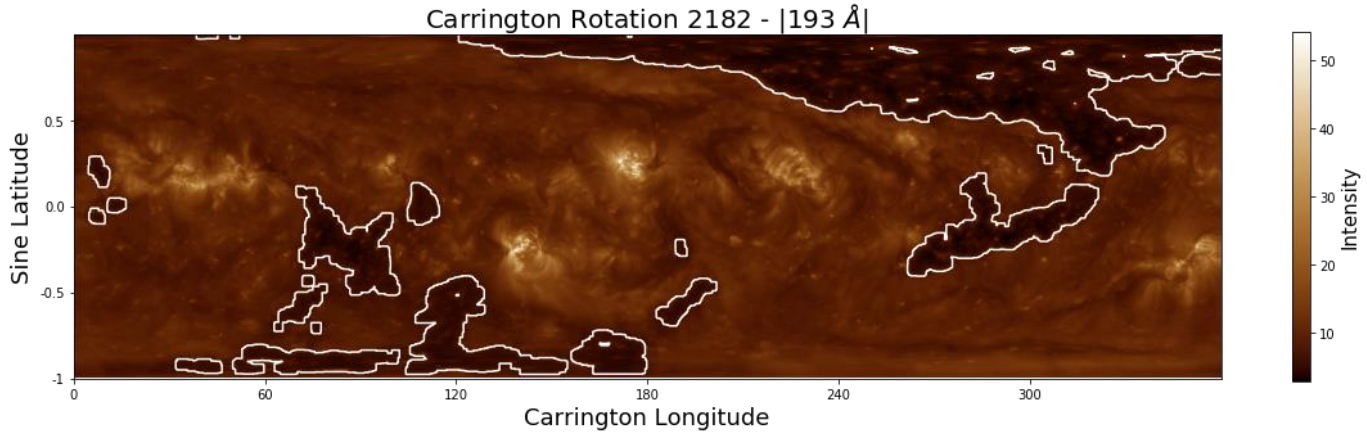

Figure 2: An EUV synoptic map of Carrington rotation 2182 with CH region contours overlaid. The contours were created by process of intensity thresholding.

positive and negative polarity. Thus, Lowder *et al.* (2014) defines regions whose magnetic field skew is greater than 0.5 in magnitude to be CHs.

With this preventative method in place, we then ran a Python loop to go through each contoured CH region and extract information like area, magnetic field, and magnetic flux to use in our analysis and comparison of CHs in cycle 23 and 24. Cycle 23 magnetic field data is SOHO/MDI data while for cycle 24 it is SDO/HMI data. According to Liu *et al.* (2012), MDI data is greater than HMI data by a factor of 1.40. We therefore, multiplied our HMI magnetic field and flux data for CRs in cycle 24 by 1.40 to make it comparable to cycle 23's MDI magnetic field data. In addition to this, the loop classified the CHs as north polar, south polar, and mid-latitude if their median latitude was greater than +60°, less than -60°, or between +60° and -60°, respectively.

RESULTS

We intended to extract data from the descending phases of solar cycles 23 and 24, spanning 28 Carrington rotations from each cycle (56 CRs total), however, due to missing EIT/MDI and AIA/MDI data, we were only able to analyze 48 CRs total. Missing data from certain CRs is noted in Figures 4 through 11 by the vertical shaded regions. In addition, it appears that the rate of evolution of cycle 24 into its minimum is accelerated compared to that of cycle 23 (this is discussed in more detail later on). This is especially apparent in the last 6 CRs. Because of this, we decided to omit data from the last 6 CRs from each cycle in our study. The omitted data is signified in Figures 4 through 11 by the yellow shaded region.

Plotted in Figure 4 is the total CH area as a percentage of the total solar surface area for both solar cycles 23 and 24. The blue points indicate total CH area percentages from CRs in cycle 23 while the red points are from CRs in cycle 24. The mean CH area

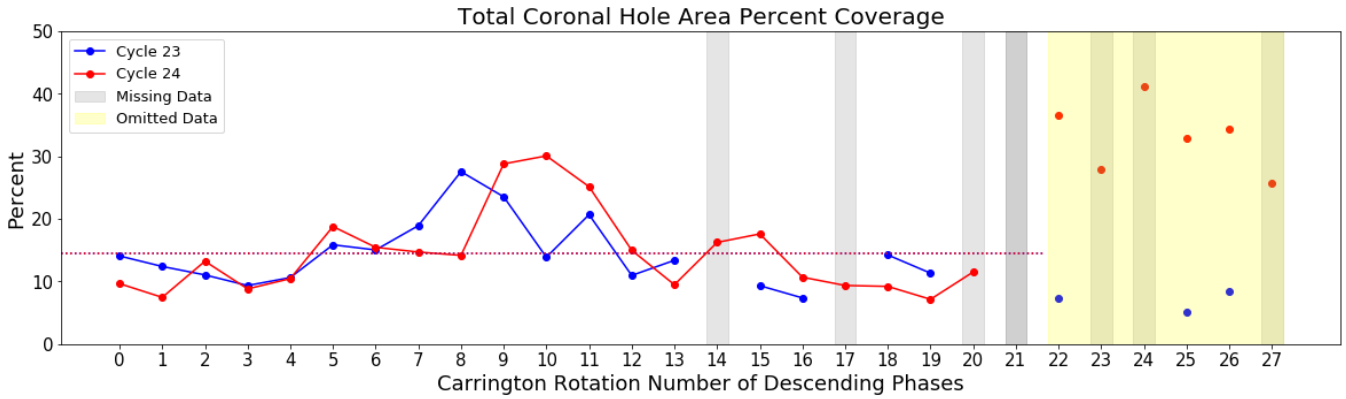

Figure 5: Plotted is the total coronal hole area percent coverage of the solar surface over the course of Carrington rotations during the descending phases of solar cycle 23 and 24. The blue notation indicates the data is from cycle 23 and the red, from cycle 24. The dashed lines indicate the mean coverage percentages for each cycle. For both cycle 23 and 24 the mean is 14.4%.

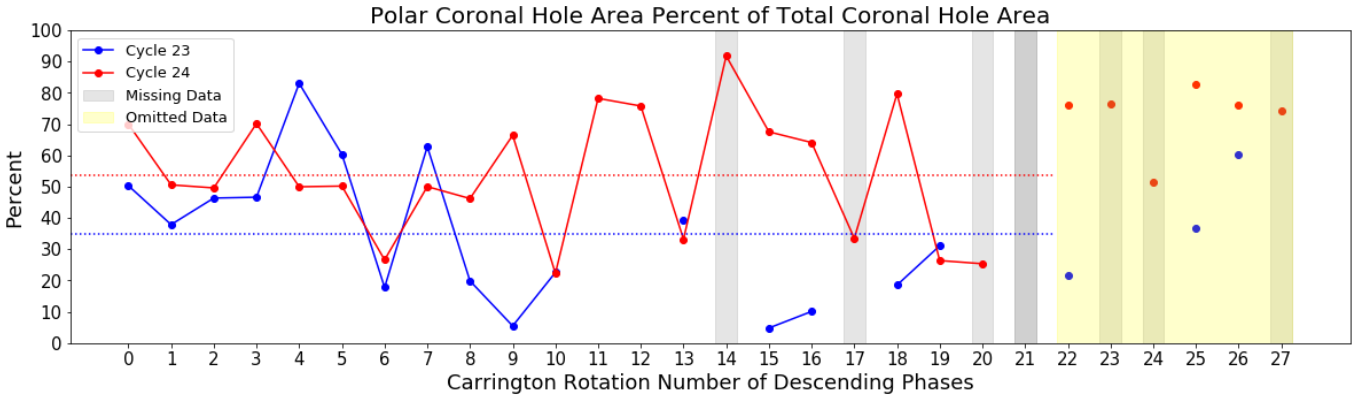

Figure 4: Plotted is polar latitude coronal hole area as a percent of total coronal hole area. For cycle 23, the mean is 34.8% and for cycle 24 the mean is 53.7%, both indicated by the dashed lines.

percent coverage in cycle 23 is 14.4% and is plotted as the blue dashed line and in cycle 24 it is also 14.4%, as the red dashed line. Because the values are significantly the same, the dashed lines lie on top of one another. These mean values as well as their standard deviations are shown in Table 1 at the end of this section.

Figure 5 shows polar CH area as a percent of total CH area during the descending phases of cycles 23 and 24. The mean polar CH area percent of total CH area for cycle 23 is 34.8% while for cycle 24 it is 53.7%. Cycle 24's descending phase has a 18.9% greater polar CH area percentage of total CH area than cycle 23. These values are also shown in Table 1 below.

We also analyzed the magnetic field and magnetic flux of CHs over the course of the descending phase of cycles 23 and 24. Figure 6, 7, and 8 show the summed and unsigned magnetic flux for northern, mid-latitude, and southern CHs, respectively. The dashed lines are the mean summed magnetic flux values for CHs at the three latitude distinctions. For north polar CHs, the mean total magnetic flux for cycle 23 is 4.16×10^21 Maxwell (Mx) (with a scaling factor of -1), while for cycle 24 it is 5.62×10^21 Mx. For mid-latitude CHs, the mean total flux for cycle 23 is 2.83×10^22 Mx and for cycle 24 it is 1.79×10^22 Mx. Lastly, for southern CHs, cycle 23 has a mean flux value of 5.41×10^21 Mx and for cycle 24 the value is 1.03×10^22 Mx (with a scaling factor of -1). All these values as well as their respective standard deviations are listed in Table 1.

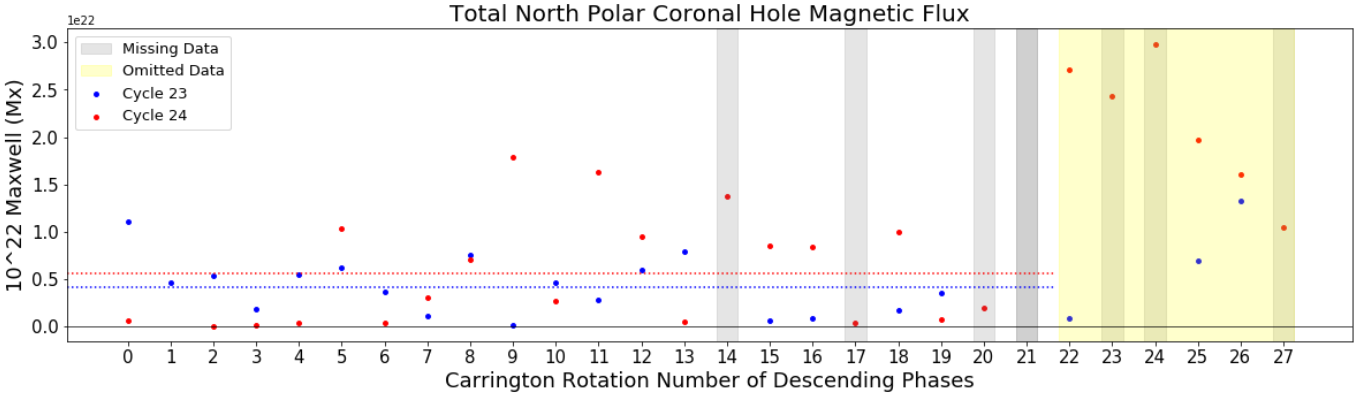

Figure 6: Plotted is the total northern latitude coronal hole magnetic flux over the course of Carrington rotations in the descending phases of solar cycle 23 and 24. The blue notation indicates the data is from cycle 23 and the red, from cycle 24. The dashed lines indicate the mean total coronal hole magnetic flux. The mean total magnetic flux of all Carrington rotations in cycle 23 is 4.16×10^21 Mx (with a scaling factor of -1) and in cycle 24 it is 5.62×10^21 Mx.

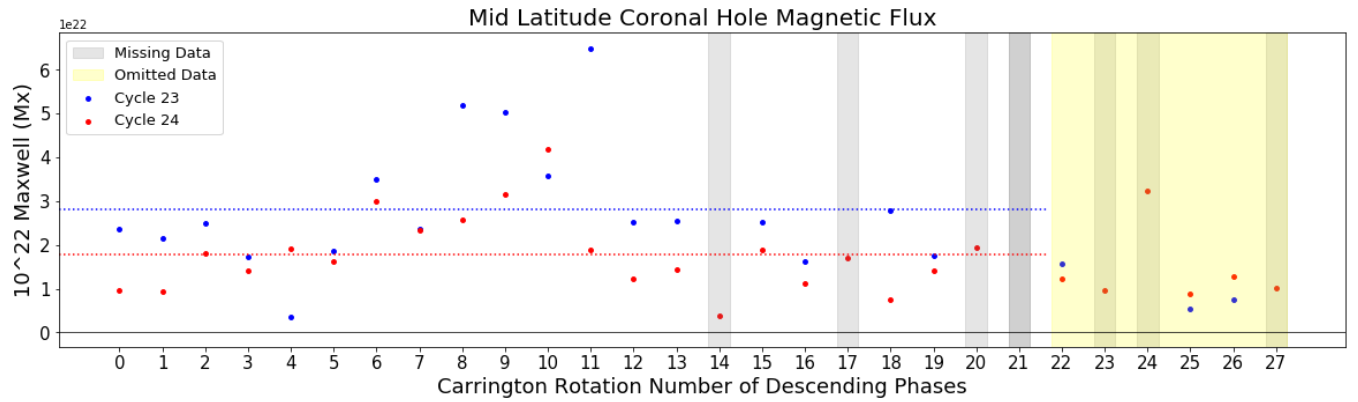

Figure 7: Plotted is the total mid-latitude coronal hole magnetic flux. The mean total flux of all Carrington rotations in cycle 23 is 2.83×10^22 Mx and in cycle 24 it is 1.79×10^22 Mx.

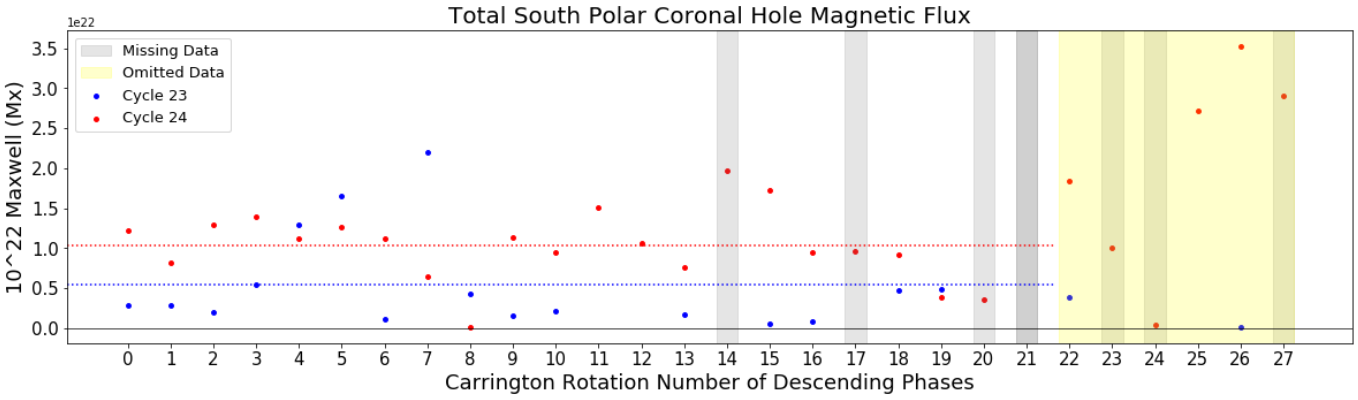

Figure 8: Plotted is the total southern latitude coronal hole magnetic flux. Cycle 23 has a mean flux value of 5.41×10^21 Mx while for cycle 24, the value is 1.03×10^22 Mx (with a scaling factor of -1).

Figures 9, 10, and 11 show the mean magnetic field magnitude of northern, mid-latitude, and southern CHs during the descending phases of the two solar cycles. Similarly, the dashed lines indicate the mean value for each cycle during their descending phases. For northern CHs, the mean magnetic field value is 3.57 Gauss (G) for cycle 23 and for cycle 24 it is 1.98 G. For mid-latitude CHs, the mean for cycle 23 is 4.65 G and for cycle 24 it is 4.48 G. For southern CHs, the mean magnetic field value is 3.14 G for cycle 23 and 4.67 G for cycle 24. These values along with the standard deviations can be found in Table 1.

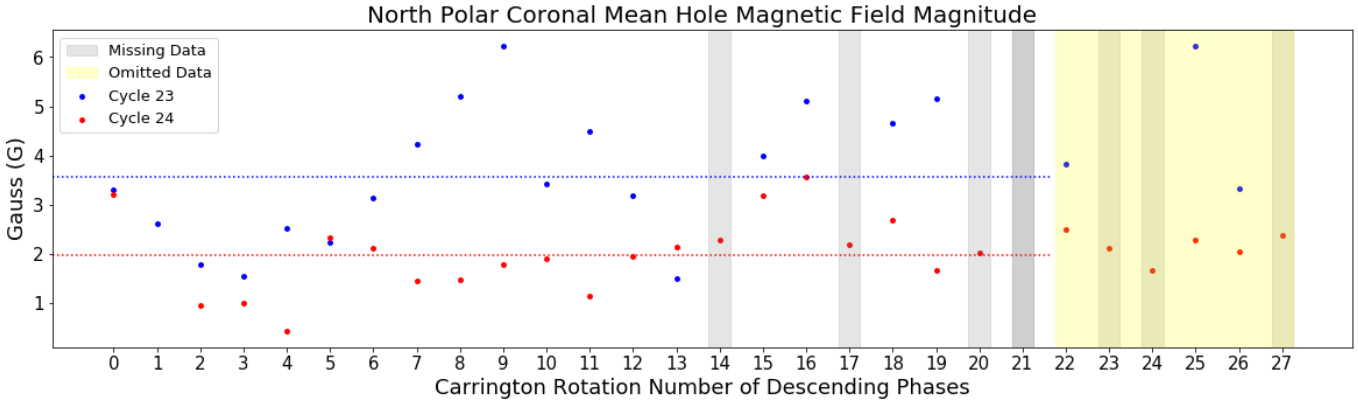

Figure 9: Plotted is northern latitude coronal hole mean magnetic field over the course of Carrington rotations in the descending phases of solar cycle 23 and 24. The blue notation indicates that the data is from cycle 23 and the red, from cycle 24. The dashed lines indicate the mean total coronal hole magnetic flux of all Carrington rotations in that cycle. For cycle 23 the mean magnetic field value is 3.57 G and for cycle 24 it is 1.98 G.

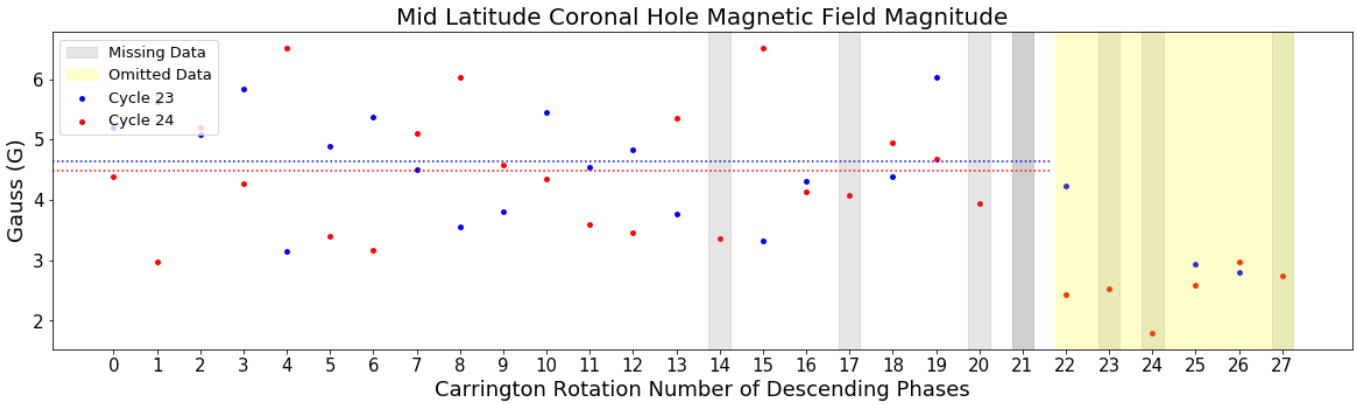

Figure 10: Plotted is the mid-latitude coronal hole mean magnetic field. The mean value from all Carrington rotations in cycle 23 is 4.65 G and for cycle 24 it is 1.98 G.

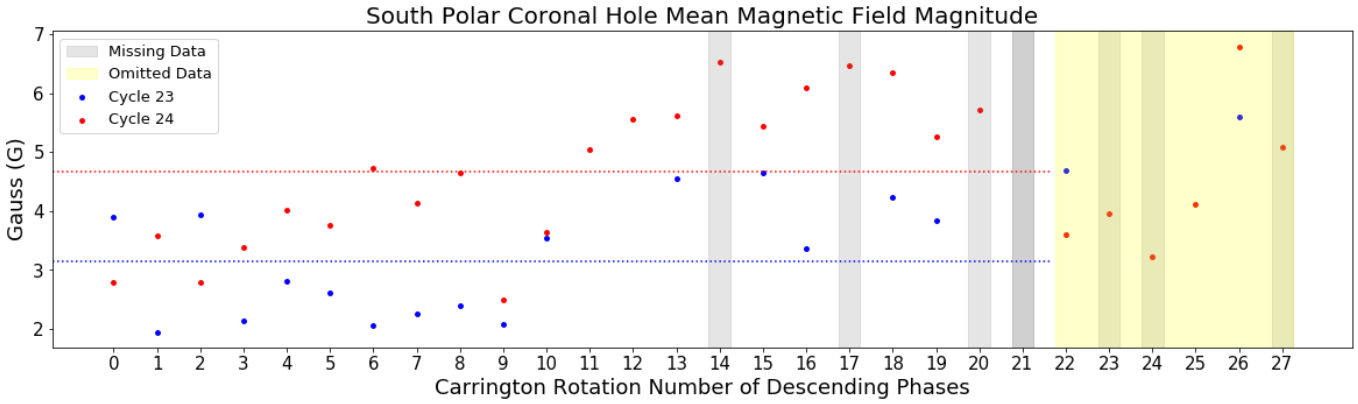

Figure 11: Plotted is the southern latitude coronal hole mean magnetic field. The mean value over all Carrington rotations in the descending phase of cycle 23 is 3.14 G and 4.67 G for cycle 24.

		Cycle 23		Cycle 24	
		mean	σ_{SD}	mean	σ_{SD}
Area (%)	Total	14.4	5.12	14.4	6.45
	Polar	34.8	21.8	53.7	20.0
Flux (unsigned total, Mx)	Northern	4.16×10^{21}	2.86×10^{21}	5.62×10^{21}	5.71×10^{21}
	Mid-Latitude	2.83×10^{22}	1.44×10^{22}	1.79×10^{22}	8.63×10^{21}
	Southern	5.41×10^{21}	6.02×10^{21}	1.03×10^{22}	4.41×10^{21}
Magnetic Field (total magnitude, G)	Northern	3.57	1.35	1.98	0.775
	Mid-Latitude	4.65	0.848	4.48	1.01
	Southern	3.14	0.929	4.67	1.25

Table 1: The mean values from Figures 4-11 and their respective standard deviations are shown. Total area is in units of percent of total solar surface area and polar area is in units of percent of total coronal hole surface area. Flux and magnetic field are in units of unsigned Maxwell and absolute Gauss, respectively.

DISCUSSION AND CONCLUDING REMARKS

Previous research has shown that solar cycle 23 had a low percentage of polar CH area and a weak magnetic dipole component as compared to the cycles preceding it (Wang *et al.* 2009.) Our research tries to reaffirm the unusual characteristics of cycle 23 but now as compared to cycle 24.

In our plots, it appears the last 6 CRs in cycle 24 were evolving into solar minimum at a more accelerated rate as compared to cycle 23. We came to this conclusion due to the sharp increases in the last 6 CRs of cycle 24 in total CH area as a percent of solar surface area and polar CH area as a percent of total CH area. A possible explanation for this is that cycle 23 and cycle 24's descending phases are not exactly in phase. To try to reduce error caused by the shift in the two descending phases, we decided to omit the data from the last 6 CRs in both cycles.

In our analysis of CH area during the descending phase, we find that the total mean CH percent coverage in cycle 24 is equal to that of cycle 23 (Figure 3). The standard deviation for cycle 24 is 6.45 while for cycle 23 it is 5.12. This means the total CH area as a percent of total solar surface area for cycle 24 is less consistent across CRs. We can assume the values would be different with a more objective methodology (discussed more at the end of this section). However, when looking at polar CH area as a percent of total CH area, the mean of cycle 24 is 18.9% greater than in cycle 23 (Figure 4). The larger percentage of CH area located at polar latitudes during the descending phase of solar cycle 24 as compared to cycle 23 indicates more area of open magnetic field situated at the solar poles. In other words, the dipole component of the solar magnetic makeup during cycle 24 is stronger than that during cycle 23.

We can investigate the possibility of this result further by looking at both magnetic flux and field magnitude during the descending phases of the two cycles. The most obvious feature of the summed flux values are their signs for the two cycle's polar CHs. All flux values are positive because for each CR, the absolute value is taken of all values, then they are summed. Cycle 23 has positive flux values at northern latitudes and would have negative at southern latitudes. For cycle 24, the polarity would be switched. This is due to the switch in magnetic poles over the course of a solar cycle. If we instead investigate the mean values of the unsigned summed fluxes, we see that for polar CHs over the descending phase, the cycle 24 mean for northern CHs was 1.46 Mx larger than that of cycle 23. However, it is difficult to argue that this difference is significant due to the fact that for cycle 24, the standard deviation is higher than the mean by roughly 0.1. For southern CHs, the mean for cycle 24 was around 1.7 times greater than that of cycle 23. For mid-latitude CHs, the mean of cycle 24 was less than that of cycle 23's by a factor of 1.5. This also supports the notion that cycle 23's dipole moment is weaker than cycle 24's. For a strong dipole moment, the flux of CHs at the pole would be much higher than the flux of CHs in the equatorial region. We see that cycle 24 has higher flux values of CHs at polar regions than cycle 23, while having lower flux values of CHs at equatorial latitudes.

When looking at magnetic field values, the conclusion is not as clearly defined. For northern CHs, the mean magnetic field magnitude for cycle 24 is 1.98 Gauss (G) and for cycle 23 it is 3.57 G. Cycle 23 has a greater mean value of northern CH magnetic field magnitude than cycle 23. The same is the case for mid-latitude CHs. For cycle 24 the mean is 4.48 G while for cycle 23 it is 4.65 G. For southern CHs, the mean magnetic field magnitude for cycle 24 is 4.67 G while for cycle 23 it is 3.14 G. The different CH latitude mean values for magnetic field magnitude do not entirely support the notion that cycle 23's dipole component is weaker than cycle 24's. The north polar CH means contradict this notion, while the south polar and mid-latitude mean values support it. This discrepancy could be due to error or could be statistically insignificant.

Overall, our methodology functions well as semi-automatic means for CH detection. This being said, there is plenty of room for improvement. The first possibility for error arises in our method of intensity thresholding. Depending on the source of the data, the EUV imagery intensity values can be scaled very differently, as discussed by Hamada 2018. To homogenize the data, one would want to perform histogram equalization, a method employed by Hamada 2018, which we did not employ in this study. Another aspect of our intensity thresholding method that may introduce error is the partial FOVs. Choosing a partial FOV for each CR was done entirely subjectively and we chose a FOV based on visually correcting for the different intensity scaling of the synoptic maps. Ideally, the selection of a partial FOV would be entirely automated and possibly done through some method of machine learning. Unfortunately, this exceeded both the scope and timeline of our project. In addition to our method of intensity thresholding, once we attained our intensity-based contoured regions, our definition of what constitutes a CH region has the potential to introduce error. Although we replicated the skew-test used by Lowder *et al.* 2014 to distinguish between CHs and filament channels, this may not be removing all unwanted low-intensity regions from our contours. For example, a region may have low intensity values in the EUV imagery, pass the skew-test (i.e. is not a filament channel), but is not a CH. These types of regions are usually very small in area (tens of pixels in width) but have high magnetic field values. These tiny, low intensity regions can add error to our mean area calculations as well as to our mean magnetic field calculations. To reduce this error, tests besides the skew-test could be implemented. For example, a minimum area threshold could reduce the number of tiny regions contoured and defined as CHs.

In terms of future research, entirely automating the process of CH contouring would reduce the error in the data extracted from EUV imagery and magnetograms as well as make the entire analysis more objective. In addition to automating our methodology, we would like to use our data to help validate CH modeling techniques, one example being the Potential Field Source Surface (PFSS) model. Comparisons of real data to modeled data would be interesting not only in the scope of bettering our understanding of solar cycle processes but also in the scope of understanding space weather and its forecasting.

REFERENCES

[1] Wang, Y.M., Robbrecht, E., Sheeley, N.R. Astrophys. J. (2009) 707:1372.
[2] Lowder, C., Qiu, J., Leamon, R., Liu, Y., Astrophys. J. (2014) 783:142.
[3] Krista, L., Gallagher, P., Sol Phys (2018) 2:06.
[4] Caplan, R.M., Downs, C., Linker, J.A. Astrophys. J. (2016) 823(1), 53.
[5] Kirk, M.S., Pesnell, W.D., Young, C.A. et al. Sol Phys (2009) 257: 99.
[6] Liu, Y., Hoeksema, J.T., Scherrer, P.H., Schou, J., Couvidat. S., Bush, R.I., Duvall, T.L., Hayashi, K., Sun, X., Zhao, X. Sol Phys (2012) 279:295.
[7] Luhmann, J.G., Li, Y., Arge C.N., Gazis, P.R., Ulrich, R. Journal of Geophysical Research (2002) 107, A8, 1154.
[8] Hamada, A., Asikainen, T., Virtanen, I., Mursula, K. Sol Phys (2018) 293:71.

ACKNOWLEDGEMENTS

We would like to acknowledge support from the Research Experience for Undergraduate program at the Institute for Astronomy, University of Hawaii-Manoa funded through NSF grant 6104374. We would also like to thank the Institute for Astronomy for their kind hospitality over the course of this project.

In addition, a special thank you to our mentor, Xudong Sun for hosting us as interns, Ben Boe for making himself available when we needed extra guidance, and to Denise Hung for helping Andrea resolve computer issues.

Lastly, we want to thank Stanford University and George Mason University for providing public and free solar data. Also, thank you to the Solar and Heliospheric Observatory and Solar Dynamic Observatory spacecraft for making solar physics research possible.